28th AIAA Applied Aerodynamics Conference
28 June - 1 July 2010, Chicago, Illinois

AIAA 2010-4552

DPW4 Results Using Different Grids Including Near-Field/Far-Field Drag Analysis

Jan B. Vos* and Stephane Sanchi†
CFS Engineering, PSE-A, 1015 Lausanne, Switzerland
Alain Gehri‡
RUAG Aviation, Center Aerodynamics, 6032 Emmen, Switzerland

CFS Engineering and RUAG Aviation participated in the 4th Drag Prediction Workshop organized by AIAA in June 2009. Calculations were made for the Common Research Model (CRM) configuration using the Navier Stokes Multi Block solver NSMB on the grids generated at CFS Engineering. After the workshop the polars were computed on the medium multi block structured grids provided by other workshop participants for the CRM configuration with zero degree horizontal tail deflection.

All these results were processed by a far field drag extraction tool developed jointly by RUAG Aviation and CFS Engineering. This paper first summarizes the theory behind the drag extraction tool. The results of the different calculations are presented and a detailed analysis of the drag breakdown on the different grids is given. This shows that the spread in drag coefficients obtained on different grids is much lower when using the effective drag computed by the drag extraction tool then when using the near field drag.

I. Introduction

DRAG prediction using Computational Fluid Dynamic (CFD) codes has been the subject of many papers and reports since the mid 1980s when computers became powerful enough to permit 3D CFD simulations. The ultimate objective is to be able to predict the drag of an aircraft within a few drag counts (where a drag count equals 10^{-4}).

The American Institute of Aeronautics and Astronautics (AIAA) organized the first Drag Prediction Workshop (DPW) in June 2001. The objectives of this first workshop were:[1]

- To assess the state-of-the-art computational methods as practical aerodynamic tools for aircraft force and moment prediction.
- To provide an impartial forum for evaluating the effectiveness of existing computer codes and modeling techniques using Navier-Stokes solvers.
- To identify areas needing additional research and development.

The test case for DPW1 was the DLR-F4 wing body configuration, measurements were made in the mid 1980ś and published in an AGARD report.[2] Standard grids were used having about 3.2 Million cells for the multi block structured grid. It was concluded that drag levels computed using CFD codes were higher than the wind tunnel results. A large scatter in drag results was observed, despite the use of standard grids.[1]

A follow on workshop was organized in 2003, with as test case the DLR-F6 wing-body-pylon-nacelle configuration.[3] The DLR-F6 was measured in August 1990 in the ONERA S2MA Wind tunnel. As for DPW1, standard grids were provided for both the Wing-Body configuration and the Wing-Body-Nacelle-Pylon configuration. The grid size was around 10 Million points for the Wing-Body and 13.7 Million points

*Director, Senior AIAA Member
†Senior Scientist, CFS Engineering
‡Senior Scientist, RUAG Aviation

for the Wing-Body-Nacelle-Pylon configuration. The results of DPW2 are summarized in.[4] It was concluded that for the Wing-Body configuration lift levels obtained using CFD were higher than wind tunnel results, drag levels were lower and the pitching moment more negative. The same conclusions were made for the Wing-Body-Nacelle-Pylon configuration except that drag levels were higher for C_L values below 0.5, and lower for higher C_L values compared to the experimental results. Compared to the results of the DPW1 workshop a reduction in spread of the results of the different contributions was observed. Several participants observed flow separations on the upper wing at the inboard trailing edge, as well as on the lower wing for the Wing-Body-Nacelle-Pylon configuration. It was believed that these flow separations were responsible for the scatter in results, and to eliminate this issue a third DPW workshop was organized in June 2006. The test cases was again the DLR-F6, but equipped with the FX2B fairing to reduce boundary layer separation at the wing body junction. In addition, two wing alone configurations were proposed. None of these configurations was tested in the wind tunnel, so DPW3 was a 'blind' CFD study. Particular attention was given on grid convergence studies since analysis of the results of the previous 2 workshops indicated that spatial discretization effects were the major source of error in the results. As a result, effects of turbulence modeling and/or transition modeling are difficult to assess. The gridding guidelines for DPW3 were adapted to permit grid convergence studies, and required a factor of about 3 in growth of the number of cells between different increasing grid levels. Results of DPW3 are among others, summarized in.[5–8]

For the DLR-F6/FX2B, the finest multi block grid used had in the order of 28 Million grid points (with respectively around 9 and 3 Million grid points for the corresponding medium and coarse grids). For the two wing alone configurations the extra fine grid had 55 Million points (with respectively around 16, 4.9 and 1.4 Million points for the fine, medium and coarse grid). Grid convergence was demonstrated by some participants for the DLR-F6/FX2B and wing alone cases.[7] The conclusions of DPW3 were that the spread in results between the different participants was of the same order as for DPW2, despite increased grid sizes, and that grid issues remained the major source of uncertainty in results.

Altough the drag prediction workshops showed a good progress in using CFD for drag prediction, predicting the drag of an aircraft configuration within a few drag counts is still a difficult job. The principal reasons that CFD codes are unable to predict the drag precisely are due to numerical and discretization errors. The drag prediction workshops clearly showed that this was the major source of uncertainty in results, before other sources as turbulence and transition modeling.

Since about 10 to 15 years, attention has been given to the development of the theory (and associated tools) for precise drag extraction from CFD simulation results. It has been shown that these tools greatly reduce the uncertainty in computed drag coefficients because these tools permit to eliminate spurious drag components generated by numerical and discretization errors from the drag.[10–12] This led to the decision by CFS Engineering and RUAG Aviation to implement such a drag extraction tool, and the theory is summarized in Section II.

Building on the success of the first 3 Drag Prediction Workshops, the 4th AIAA Drag Prediction Workshop (DPW4) was organized in June 2009. The test case selected for for DPW4 is the NASA Common Research Model (CRM),[9] which is a wing-body-nacelle-pylon-horizontal tail configuration. The different CRM configurations considered for DPW4 and the computation matrix are briefly summarized in Section III. CFS Engineering and RUAG Aviation performed calculations on our own grid. After the workshop it was decided to compute the polar for the CRM with zero degree horizontal tail deflection using all available multi block structured grids, and to use the drag extraction analysis tool for the analysis of the different drag components. The results of this analysis are summarized in Section IV.D.

II. Theory Far-field Drag Extraction

II.A. Integral Momentum Balance

The theoretical foundation of the so called 'far field' or 'mid field' drag extraction methods can be found in the report by Van der Vooren and Slooff.[13] This work was further developed by Destarac[10] and Tognaccini.[14] A good theoretical discussion can be found in the thesis of Esquieu.[15] A general overview of drag prediction methods is given by Van Dam.[16]

Consider a steady flow with free-stream velocity $\mathbf{V}_\infty$ around an aircraft. The integral momentum balance for a closed volume Ω with surface S surrounding the aircraft and located far from the aircraft yields:[14]

$$\int_{\mathrm{S}} [\rho \mathbf{V}\mathbf{V} + p\mathbf{U} - \tau] \cdot \mathbf{n} dS = \int_{\mathrm{S}} [\rho \mathbf{V}\mathbf{V} + (p - p_\infty)\mathbf{U} - \tau] \cdot \mathbf{n} dS = 0 \tag{1}$$

In this equation ρ, p, $\mathbf{V}$, and τ are respectively the density, pressure, velocity vector and shear stress tensor, while the subscript ∞ indicates free stream values. $\mathbf{U}$ is the unit tensor, $\mathbf{n}$ is the unit normal vector pointing outside the volume Ω and S is the surface bounding the volume Ω. The surface S can be decomposed in S_{far} and S_{body} where S_{far} is the surface surrounding the far field and S_{body} the surface surrounding the body. In the case of a no-slip or tangential flow on the body walls $\mathbf{V} \cdot \mathbf{n} = 0$ on S_{body} and Eq. 1 can be written as

$$\mathbf{F} = \int_{\mathrm{S_{body}}} [(p - p_\infty)\ \mathbf{n} - \tau \cdot \mathbf{n}]\, dS = - \int_{\mathrm{S_{far}}} [\rho \mathbf{V}\mathbf{V} + (p - p_\infty)\mathbf{U} - \tau] \cdot \mathbf{n} dS \tag{2}$$

with $\mathbf{F}$ the total force the fluid acts on the body (assuming an un-powered aircraft). Equation 2 shows that the total force can be computed in two different ways:

1. compute the integral of the pressure and shear stresses acting on the aircraft surface: *near field integration*
2. calculate the momentum flux balance on the outer boundaries of the calculation domain: *far field integration*.

Assuming the coordinate system aligned with the free stream velocity, then the total aerodynamic drag is the x-component of the force vector $\mathbf{F}$. For the far field integration this gives

$$D_{far} = - \int_{\mathrm{S_{far}}} [(p - p_\infty)n_x + \rho u(\mathbf{V} \cdot \mathbf{n}) - \tau_{xx}n_x - \tau_{xy}n_y - \tau_{xz}n_z]\, dS \tag{3}$$

with u the velocity component aligned with the x-axis of the aerodynamic frame. Since the surface is closed, this equation can also be written as:

$$D_{far} = - \int_{\mathrm{S_{far}}} [(p - p_\infty)n_x + \rho(u - u_\infty)(\mathbf{V} \cdot \mathbf{n}) - \tau_{xx}n_x - \tau_{xy}n_y - \tau_{xz}n_z]\, dS \tag{4}$$

Define the vector $\mathbf{f}$ as

$$\mathbf{f} = -\rho(u - u_\infty)\mathbf{V} - (p - p_\infty)\mathbf{n} + \tau_{\mathbf{x}} \tag{5}$$

Then Eq. 4 can be written as

$$D_{far} = \int_{\mathrm{S_{far}}} (\mathbf{f} \cdot \mathbf{n}) dS \tag{6}$$

and from Eq. 2 , the far field drag D_{far} should equal the near field drag D_{nf},

$$D = D_p + D_f = \int_{\mathrm{S_{far}}} (\mathbf{f} \cdot \mathbf{n}) dS \tag{7}$$

with D_p the drag due to pressure forces and D_f the drag due to friction forces on the body.

The far field integration permits a break down of the total drag into its physical components: viscous drag, wave drag, induced drag and an additional component called spurious drag that is introduced by the numerical method. This physical breakdown is based on a distinction between thermodynamic irreversible and reversible processes.[13] Viscous and wave drag are irreversible processes, while induced drag is an exchange of energy and is thus reversible.

II.B. Thermodynamic Variables

To study the different drag components it is needed to introduce several thermodynamic variables. The variation of the entropy (Δs) with respect to the free stream state equals

$$\Delta s = \frac{R}{(\gamma-1)} log\left[\frac{p}{p_\infty}\left(\frac{\rho_\infty}{\rho}\right)^\gamma\right] \tag{8}$$

with R the gas constant and γ the ratio of specific heats. The variation of the stagnation enthalpy relative to the free stream is given as

$$\Delta H = H - H_\infty = \frac{\gamma}{(\gamma-1)}\left(\frac{p}{\rho} - \frac{p_\infty}{\rho_\infty}\right) + \frac{u^2+v^2+w^2}{2} - \frac{u_\infty^2}{2} \tag{9}$$

In this equation u, v and w are the velocity components in the aerodynamic frame (aligned with the free stream velocity).

Combining Eqs. 8 and 9 together with the equation of state permits to express the pressure as function of Δs, ΔH and the velocity components[10,14]

$$\frac{p}{p_\infty} = e^{-\frac{\Delta s}{R}}\left(1 + \frac{(\gamma-1)M_\infty^2}{2}\left[1 - \frac{u^2+v^2+w^2}{u_\infty^2} + 2\frac{\Delta H}{u_\infty^2}\right]\right)^{\left(\frac{\gamma}{\gamma-1}\right)} \tag{10}$$

From this equation one can obtain the ratio of velocity components in x-direction:

$$\frac{u}{u_\infty} = \sqrt{1 + 2\frac{\Delta H}{u_\infty^2} - \frac{2}{(\gamma-1)M_\infty^2}\left[\left(\frac{\Delta p}{p_\infty}+1\right)^{\frac{(\gamma-1)}{\gamma}} e^{\frac{\Delta s}{R}\frac{(\gamma-1)}{\gamma}} - 1\right]} = f\left(\frac{\Delta p}{p_\infty}, \frac{\Delta s}{R}, \frac{\Delta H}{u_\infty^2}\right) \tag{11}$$

It should be stressed that Eqs. 10 and 11 are valid only in the aerodynamic frame (aligned with the free stream velocity). Equation 11 can be expanded in a Taylor's series[14] resulting in:

$$\begin{aligned}\frac{u}{u_\infty} = 1 \quad &+ \quad f_{fp1}\frac{\Delta p}{p_\infty} + f_{fs1}\frac{\Delta s}{R} + f_{fH1}\frac{\Delta H}{u_\infty^2} \\ &+ \quad f_{fp2}\frac{\Delta p}{p_\infty} + f_{fs2}\frac{\Delta s}{R} + f_{fH2}\frac{\Delta H}{u_\infty^2} \\ &+ \quad f_{fps2}\frac{\Delta p}{p_\infty}\frac{\Delta s}{R} + f_{fpH2}\frac{\Delta p}{p_\infty}\frac{\Delta H}{u_\infty^2} + f_{fsH2}\frac{\Delta s}{R}\frac{\Delta H}{u_\infty^2} \\ &+ \quad O\left[\left(\frac{\Delta p}{p_\infty}\right)^3, \left(\frac{\Delta s}{R}\right)^3, \left(\frac{\Delta H}{u_\infty^2}\right)^3\right]\end{aligned} \tag{12}$$

The coefficients of the series expansion depend on γ and M_∞, and are for the first and second order terms written as:

$$\begin{aligned} f_{fp1} &= -\frac{1}{\gamma M_\infty^2}, & f_{fs1} &= -\tfrac{1}{\gamma M_\infty^2}, & f_{fH1} &= 1 \\ f_{fp2} &= -\frac{1+\gamma M_\infty^2}{2\gamma^2 M_\infty^4}, & f_{fs2} &= -\tfrac{1+(\gamma-1)M_\infty^2}{2\gamma^2 M_\infty^4}, & f_{fH2} &= -\frac{1}{2} \\ f_{fps2} &= -\frac{1+(\gamma-1)M_\infty^2}{\gamma^2 M_\infty^4}, & f_{fpH2} &= \tfrac{1}{\gamma M_\infty^2}, & f_{fsH2} &= \frac{1}{\gamma M_\infty^2} \end{aligned} \tag{13}$$

II.C. Viscous and Wave Drag Components

Viscous and wave drag are irreversible phenomena, and are connected to the terms with entropy production in Eq. 12. Using a perturbation approach assuming $\frac{\Delta s}{R} << 1$ and $\frac{\Delta H}{u_\infty^2} << 1$, it is possible to write the irreversible drag as[10,15]

$$D_{irrev} = -\int_{S_{far}} \rho(u-u_\infty)(\mathbf{V}\cdot\mathbf{n})dS = -\int_{S_{far}} \rho\Delta u(\mathbf{V}\cdot\mathbf{n})dS = \int_{S_{far}} \mathbf{f_{vw}}\cdot\mathbf{n}dS \tag{14}$$

The downstream plane S_{far} is sufficiently far from the body to assume that $p = p_\infty$ and the shear stresses equal zero. The function f_{vw} is defined as

$$\mathbf{f_{vw}} = -\rho\Delta u\mathbf{V} \tag{15}$$

In this equation Δu represents the velocity deficit in longitudinal direction *due to irreversible phenomena*. Equation 14 contains surface integrals over the computational domain. Upstream of the body, the flow is unperturbed, the pressure equals the free stream pressure and the velocity equals the free-stream velocity. As a result, the surface integral can be replaced by an integral over the down stream surface, where this surface should be sufficiently far from the body.

Integration of Eq. 14 over the down stream surface does not permit to separate the irreversible drag into a viscous and wave drag component. However, transforming the surface integral in a volume integral permits this separation. Equation 3 is written as follows:

$$D_{irrev} = D_v + D_w = \int_{S_{far}} \mathbf{f_{vw}}\cdot\mathbf{n}dS = \int_V div\mathbf{f_{vw}}dV \tag{16}$$

where D_v is the viscous and D_w the wave drag. Since irreversible processes are only important in viscous and shock regions, one can limit the volume integral in Eq. 16 to these regions:

$$\begin{aligned} D_v &= \int_{V_v} div\mathbf{f_{vw}}dV \\ D_w &= \int_{V_w} div\mathbf{f_{vw}}dV \end{aligned} \tag{17}$$

To detect these regions the sensors defined by Tognaccini[14] are used. For the shock region

$$f_{shock} = \frac{\mathbf{V}\cdot\nabla p}{a|\nabla\, p|} \tag{18}$$

with a the local speed of sound. f_{shock} is larger then zero in compression regions, and when $f_{shock} > 1$ the finite volume cell is in the region of a shock wave. Using the Rankine-Hugoniot relations it is possible to make an estimation of the Mach number downstream of the shock. This permits the calculation of a cutoff constant K_{cw} which is used for the selection of the region downstream of the shock.

$$k_{cw} = \sqrt{\frac{(1+0.5(\gamma-1)f^2_{shock_{max}})}{(\gamma f^2_{shock_{max}} - 0.5(\gamma-1)}} \tag{19}$$

with $f_{shock_{max}}$ the maximum value of f_{shock} in the flow field.

For the detection of the wake and boundary layer region a sensor based on the use of the turbulent viscosity is used:[14]

$$f_v = 1 + \left(\frac{\mu_t}{\mu_l}\right) \tag{20}$$

with μ_l and μ_t respectively the laminar and turbulent viscosity. A finite volume cell belongs to the viscous region if the $f_v > k_{bl} f_{v_\infty}$ with k_{bl} a cut off constant in general set to 1.1.

Esquieu[15] uses a different method based on the norm of the shear stress tensor at the cell center of a finite volume cell. If this norm is larger than a cutoff constant k_τ times the maximum norm in the boundary layer then the cell belongs to the viscous region. The cutoff constant k_τ is in general set to 0.02. It was observed that both criteria were not sufficient to attribute cells in the laminar sub region to the viscous region. For this reason a third criteria was added based on the wall distance and attributes all cells with an y^+ value lower than 20 to the viscous region.

II.D. Induced Drag

INDUCED drag is generated by the lift of the body due to the a vortex at the wing tip. The **classical method** to compute the induced drag is by considering the wake plane sufficiently far from the body to assume $\tau_{\mathbf{x}}$ equals zero and Eq. 4 then becomes

$$D_i = \int_{S_{far}} [(p_\infty - p)\mathbf{U} + \rho(u_\infty - u)\mathbf{V}] \cdot \mathbf{n} dS \tag{21}$$

Far down stream of the body the velocity vector can be approximated as

$$\mathbf{V} = u_\infty \left((1 + \Delta u), \Delta v, \Delta w\right)^T \tag{22}$$

where Δu is the velocity difference due to reversible phenomena ($u - u_\infty - \Delta u_{irrev}$). Using the definition of the speed of sound Eq. 21 is written as

$$D_i = \rho_\infty u_\infty^2 \int_{S_{far}} \left[\frac{1}{\gamma M_\infty^2}(1 - \frac{p}{p_\infty})\mathbf{U} - \Delta u(\frac{\rho}{\rho_\infty})(\frac{\mathbf{V}}{u_\infty})\right] \cdot \mathbf{n} dS \tag{23}$$

THE pressure ratio can be found from thermodynamics, see Eq. 10. Since the induced drag is a reversible process, it follows that Δs in this equation can be set to zero, and ΔH can be set to zero as well since no external energy is provided. Substituting the resulting equation in Eq. 21 yields[15]

$$\begin{aligned} D_i \quad = \quad & \rho_\infty u_\infty^2 \int_{S_{far}} \left[\frac{1}{\gamma M_\infty^2}\left(1 - \left[1 + \frac{1}{2}(\gamma - 1)M_\infty^2(1 - \frac{u^2 + v^2 + w^2}{u_\infty^2})\right]^{\frac{\gamma}{(\gamma-1)}}\right)\mathbf{U}\right. \\ & \left. -\Delta u \left[1 + \frac{1}{2}(\gamma - 1)M_\infty^2(1 - \frac{u^2 + v^2 + w^2}{u_\infty^2})\right]^{\frac{1}{(\gamma-1)}} \frac{\mathbf{V}}{u_\infty}\right] \cdot \mathbf{n} dS \end{aligned} \tag{24}$$

Substitution of Eq. 22 and using the fact that $\Delta u << 1$, $\Delta v << 1$, $\Delta w << 1$ one obtains the classical equation for the induced drag

$$D_i = \rho_\infty u_\infty^2 \int_{S_{far}} \left(\frac{1}{2}\left[\Delta v^2 + \Delta w^2 - (1 - M_\infty^2)\Delta u^2\right] n_x - (\Delta u \Delta v) n_y - (\Delta u \Delta w) n_z\right) \cdot \mathbf{n} dS \tag{25}$$

THE velocity difference Δu corresponds to the change in horizontal velocity and there are 2 phenomena responsible for this: irreversible and reversible. Only reversible phenomena can contribute to the induced drag. Equation 11 (or its Taylor series expansion Eq. 12) can be used to separate the velocity difference in a reversible and irreversible part.

This is not further elaborated since a **new formulation** of the induced drag was developed by Van der Vooren.[13] Starting from the definitions of the vectors $\mathbf{f}$ and $\mathbf{f_{vw}}$, one can write

$$\mathbf{f} = \mathbf{f_{vw}} + \mathbf{f_i} \tag{26}$$

with $\mathbf{f_i}$ the force due to the induced drag. Using the definitions of $\mathbf{f}$ (Eq. 5) and $\mathbf{f_{vw}}$ (Eq. 15) one obtains

$$\mathbf{f_i} = -\rho(u - u_\infty - \Delta u)\mathbf{V} - (p - p_\infty)\mathbf{n} + \tau_{\mathbf{x}} \tag{27}$$

The induced drag can thus be obtained by integrating Eq. 27 over the far-field planes,

$$D_i = -\int_{S_{far}} \mathbf{f_i} \cdot \mathbf{n} dS \tag{28}$$

HOWEVER, integration of Eq. 28 over the far-field plane poses several problems. First one needs to construct the wake plane, which is not trivial. Secondly part of the lift induced drag is converted in artificial viscous drag due to the numerical scheme and the grid employed in the wake. For this reason it is desirable to place the wake plane as close to the body as possible.

To solve these problems a new approach was proposed based on the volume integration of Eq. 27 over the computational domain

$$D_i = \int_{\mathrm{V}} div\mathbf{f_i} dV - \int_{\mathrm{S_A}} \mathbf{f_i} \cdot \mathbf{n} dS \tag{29}$$

The integration volume V in this equation can be replaced by the integration over the shock and viscous regions.[11]

Equation 29 has several distinct advantages. First since $\mathbf{f_{vw}} \cdot \mathbf{n}$ equals zero on the surface of the body S_A it follows that the surface integral can be written as

$$-\int_{\mathrm{S_A}} \mathbf{f_i} \cdot \mathbf{n} dS = -\int_{\mathrm{S_A}} \mathbf{f} \cdot \mathbf{n} dS = D_p + D_f \tag{30}$$

where use has been made of Eq. 7. Another observation is that $div\mathbf{f} = div(\mathbf{f_{vw}} + \mathbf{f_i}) = 0$ from which follows that

$$div\mathbf{f_{vw}} = -div\mathbf{f_i} \tag{31}$$

Combining Eqs. 29 and 30 and using Eq. 31 yields the exact relation between near field and far field drag

$$D_p + D_f = D_i + D_v + D_w \tag{32}$$

FOLLOWING Eq. 31 it is possible to use the vector $\mathbf{f_i}$ in the calculation of the viscous and wave drag, Eq. 17, and results from Destarac[10] and Esquieu[15] indicate that this is the preferred method because $\mathbf{f_i}$ has a more smooth behavior in the flow field than $\mathbf{f_{vw}}$.

Equation 32 is exact, but when making numerical simulations spurious numerical drag may appear in the solution. This drag component is due to the quality of the grid and the artificial dissipation of the numerical scheme employed. Equation 32 can be written as

$$D_p + D_f = D_i + D_v + D_w + D_{sp} \tag{33}$$

with D_{sp} the spurious drag, defined as the difference between near field drag on one hand, and the sum of viscous, wave and induced drag on the other hand. The spurious drag is irreversible, and is generated in the cells outside the viscous and wave regions,

$$D_{sp} = \int_{\mathrm{V_{sp}}} div\mathbf{f_{vw}} dV \tag{34}$$

To satisfy the near field - far field drag balance, it is now necessary to include the spurious region in the calculation of the induced drag.

II.E. Correction procedures

NUMERICAL schemes in general do not have very fine meshes in the wake region. As a result, wake vortices are quickly diffused and the induced drag is reduced due to a transfer of induced to viscous drag. Correction procedures have been developed,[10,15] which consists of integration Eq. 15 over a so called correction volume. This correction volume is a cone starting at the wing tip until the down stream integration plane.

It can be advantageous to limit the volume integration in down stream direction up to a wake plane located downstream of the geometry. In practice this wake plane is placed at 5% the body length downstream of the geometry.

Another issue is the question where to start and stop the volume integration. Experience from several calculations showed that starting at the far-field boundary may introduce numerical errors, leading to a wrong induced drag. In practice the far field drag integration volume is reduced by ignoring a certain number of rows of grid cells (in practice about 10) from the far field boundary.

II.F. Alternative Formulations

Several alternative formulations exist, based on the use of different methods and strategies to compute the induced drag. Besides using the method discussed before, Esquieu[12] also computes the induced drag from Eq. 25 with the velocity difference Δu calculated from

$$\Delta u = u - u_\infty + u_\infty \left(\frac{1}{\gamma M_\infty^2} \frac{\Delta s}{R} - \frac{\Delta H}{u_\infty^2} \right) \tag{35}$$

The main difference with the standard method is the use of the classical formulation for the induced drag, and that only first order terms are taken into account when computing the velocity difference.

Yamazaki[17,18] computes the induced drag from Eq. 25 integrated over a plane in the wake normal to the flow direction.

For both these methods the effective drag is the sum of viscous, wave and induced drag, and the spurious drag becomes the difference between near field and effective drag.

III. DPW4 Workshop

III.A. Experimental Test Case

The test case selected for DPW4 is the NASA Common Research Model (CRM),[9] which is a wing-body-nacelle-pylon-horizontal tail configuration, see Fig. 1 for a picture of the CRM without nacelle and pylon.

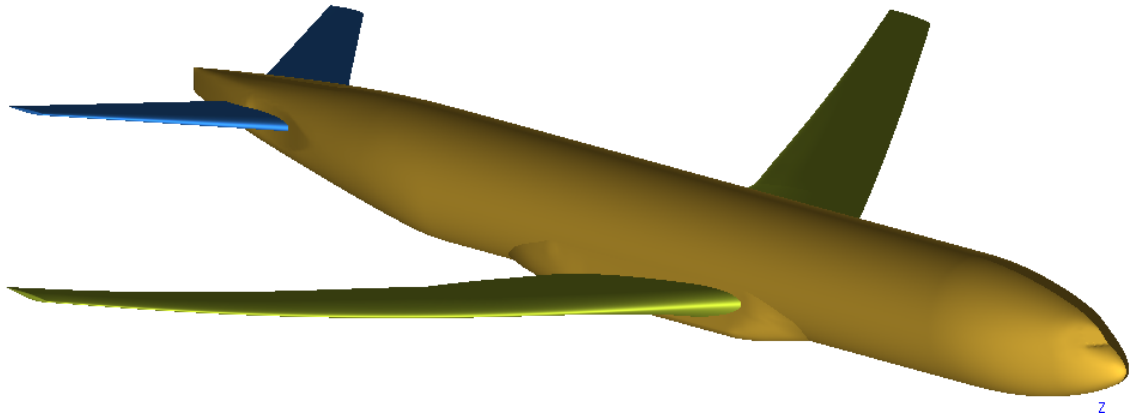

Figure 1. Common Research Model without nacelle-pylon.

The CRM is the result of a request from different parties asking NASA to develop an experimental data base for a contemporary aircraft configuration for the use of CFD validation.[9] The Boeing Company was responsible for the detailed aerodynamic design of the CRM, while the NASA Fundamental Aerodynamics/Subsonic Fixed Wing Project took the lead on the model design, fabrication and testing. The wing of the CRM is a transonic supercritical wing with high performance for configurations with and without nacelle and pylon. The horizontal tail has a robust design and is suitably designed for stability and control requirements. The fuselage is that of a wide body commercial aircraft and includes a wing-body fairing and a scrubbing seal for the horizontal tail.

The CRM is representative of a transonic aircraft designed to fly at a cruise Mach number of 0.85 with a nominal lift coefficient of 0.5 and a Reynolds number of 40 Million per reference chord. The reference quantities of the CRM are summarized in Table 1, both in American and SI units.

The wing position of the CRM corresponds to a nominal 1-G wing at cruise. The trailing-edge thickness of the wing is non zero to accommodate a model fabrication constraint. A picture of the wing is shown in Fig. 2. A large number of requirements was imposed on the CRM design, among them a high performance around the design point, possibility to accommodate a 1.3G to buffet criteria and good aerodynamic performance with and without nacelle-pylon. Measurements can be made with and without horizontal tail. If a horizontal tail is present it can be mounted using 3 trail incidence angles ($0^o, \pm 2^o$), to determine the trimmed condition.

	American Units	SI-Units
S_{ref}	594'720 in^2	383.690 m^2
C_{ref}	275.80 in	7.00532 m
Span	2313.5 in	58.7629 m
X_{ref}	1325.9 in	33.67786m
Y_{ref}	468.75 in	11.90625m
Z_{ref}	177.95 in	4.51993m
λ	0.275	0.275
$\Lambda_{C/4}$	35^o	35^o
AR	9.0	9.0

Table 1. Reference Parameters Common Research Model.

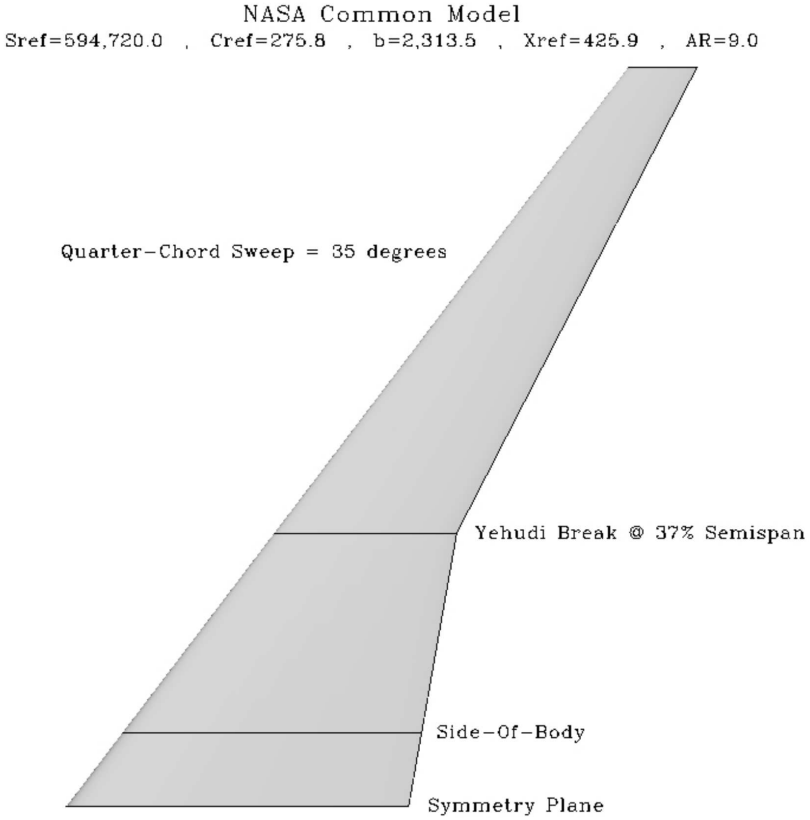

Figure 2. Common Research Model Wing.

EXPERIMENTAL testing of the CRM was scheduled to take place by the end of 2009 in the NASA National Transonic Facility (NTF) at Langley and in 2010 in the NASA Ames 11-ft transonic wind tunnel. The NASA Ames facility will provide skin friction data at a low Reynolds number, while measurements at the NTF include cryogenic runs for high Reynolds number data. Mach numbers to be measured varied between 0.70 and 0.92, with particular focus on the design point of Mach 0.85. The CRM has on the wing 303 pressure stations at 8 span wise locations. Pressure tabs are distributed between the left and right wing to minimize differences due to asymmetric twist or bending.

MEASURED data consists of force, moment, and surface pressure, plus wing deformation under load. Velocity fields obtained using PIV will be measured in the NASA Ames facility as well as skin-friction data.

III.B. CFD Test Cases

Three different computational test cases were defined for DPW4, of which Case 2 and Case 3 were optional.

III.B.1. Case 1a: Grid Convergence study

Case 1a concerned a grid convergence study at $Mach = 0.85$, $C_L = 0.500$ (± 0.001) for the configuration with 0^o tail incidence. The chord Reynolds number was 5 10^6 using a reference chord length of $C_{ref} = 275.80\ in.$ For this case the total reference temperature was 100 $Fahrenheit$.

A minimum of 3 grids were to be used, with a fine grid of around 35 Million points, a medium grid of 10 Million points and a coarse grid of 3.5 Million points. An optional extra fine grid of 100 Million points could be used too.

Table 2 summarizes the free stream conditions in SI units.

$Mach$	0.85	
p_{tot}	201326.91	Pa
T_{tot}	310.92778	K
$Reynolds$	7.1374 10^5	$1/m$

Table 2. DPW4 free stream conditions in SI units.

III.B.2. Case 1b: Downwash study

Case 1b concerned a downwash study at $Mach = 0.85$ by computing drag polars on the medium grid for $\alpha = 0.0^o, 1.0^o, 1.5^o, 2.0^o, 2.5^o, 3.0^o, 4.0^o$ for the DPW4 configurations without horizontal tail, and with tail incidence angles $i_H = -2^o, 0^o, 2^o$. Free stream total pressure and total temperature are given in Table 2.

III.B.3. Case 2: Mach Sweep study

Case 2 concerned calculations using the medium grid on the configuration with $i_H = 0.0^o$ for $C_L = 0.4, 0.45, 0.5$ (± 0.001) at $Mach = 0.70, 0.75, 0.80, 0.83, 0.85, 0.86, 0.87$. Free stream total pressure and total temperature are given in Table 2.

III.B.4. Case 3: Reynolds number study

Case 3 concerned calculations using the medium grid on the configuration with $i_H = 0.0^o$ for $C_L = 0.5$ (± 0.001) at Reynolds numbers of 5 10^6 and 20 10^6. Free stream total pressure and total temperature are given in Table 2.

IV. Results

IV.A. NSMB Solver Parameters

All calculations reported in this paper were made using the Navier Stokes Multi Block solver NSMB.[19,20] A 4th order central scheme with artificial dissipation was used for the space discretization, and the semi implicit LU-SGS scheme for the time integration. The CFL number was increased to 10^{12} during the time integration process. When possible two levels of full multi grid (grid sequencing) were used. Turbulence was modeled using the $k - \omega$ Menter Shear Stress turbulence model.[21]

IV.B. Grid Convergence Study

Calculations were made on a coarse, medium and fine grid generated by cfse-ra having respectively 3.78, 11.36 and 39.96 million grid points, and Table 3 summarizes the computed results, with C_{D_p} and C_{D_f} respectively the drag due pressure forces and skin frictions forces on the body, C_{D_v} and C_{D_w} respectively the viscous and wave drag, $C_{D_{NF}}$ the near field drag and $C_{D_{eff}}$ the effective drag for both Volume integration (V) and integration upto a wake plane (W).

grid	α	C_L	C_{D_p}	C_{D_f}	$C_{D_{NF}}$	C_{D_v}	C_{D_w}	$C_{D_{eff}V}$	$C_{D_{eff}W}$	C_{M_y}
crs	2.406	0.5010	220	128	348	234	6	305	304	-0.0632
med	2.381	0.5007	178	132	309	204	15	283	282	-0.0535
fine	2.413	0.5003	172	126	298	196	15	279	277	-0.0379

Table 3. DPW4 results grid convergence study, drag values in drag counts.

Figure 3 shows the grid convergence for the idealized drag coefficient defined as $C_D - {C_L}^2/(\pi AR)$ with AR the aspect ratio. The idealized drag is plotted in drag counts for the near field and effective drag.

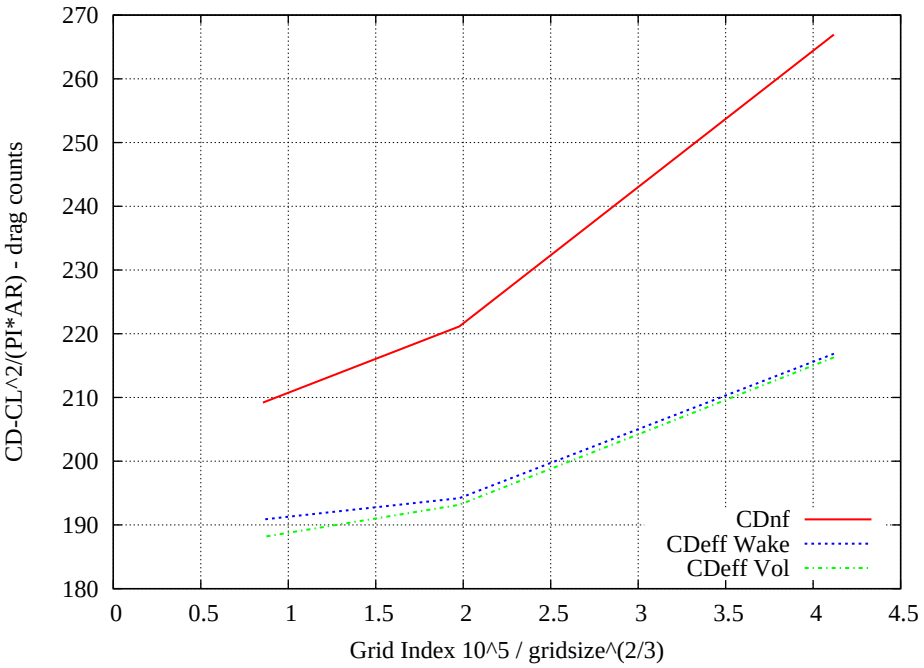

Figure 3. Grid convergence near field and effective drag.

As can be seen from Fig. 3, the slopes of the grid convergence for near field and effective drag differ, and the effective drag converges faster. For the effective drag computed using the integration until a wake plane, the difference in drag on medium and fine grid is less than 4 drag counts, while it is around 11 drag counts for the near field drag. Looking at the different components of the effective drag, one observes that the viscous drag is slightly reduced when going from medium to fine grid, but the induced drag is increased due to a better capturing of wing tip vortex.

IV.C. Down wash study

FIGURE 4 shows the computed idealized drag polars for the down wash study with the C_D based on the near field drag and on the effective drag. Comparing the polars based on near field and effective drag shows a reduction of about 20 drag counts when using the effective drag. At the same time the different drag polars are closer to each other, for low values of the C_L the difference in $C_{D_{ideal}}$ is about 24 drag counts when using the near field drag and about 20 drag counts when using the effective drag.

IV.D. Analysis of Results obtained on different Grids

FIVE other participants in the DPW4 workshop provided multi block structured grids, and it was decided to compare results obtained with the cfse-ra grid for the 0^o deflected horizontal tail with results obtained using these other grids. Table 4 summarizes some of the characteristics of the different grids used. The Airbus grid was in CGNS format, converting this grid gave some minor problems due to some ambiguities

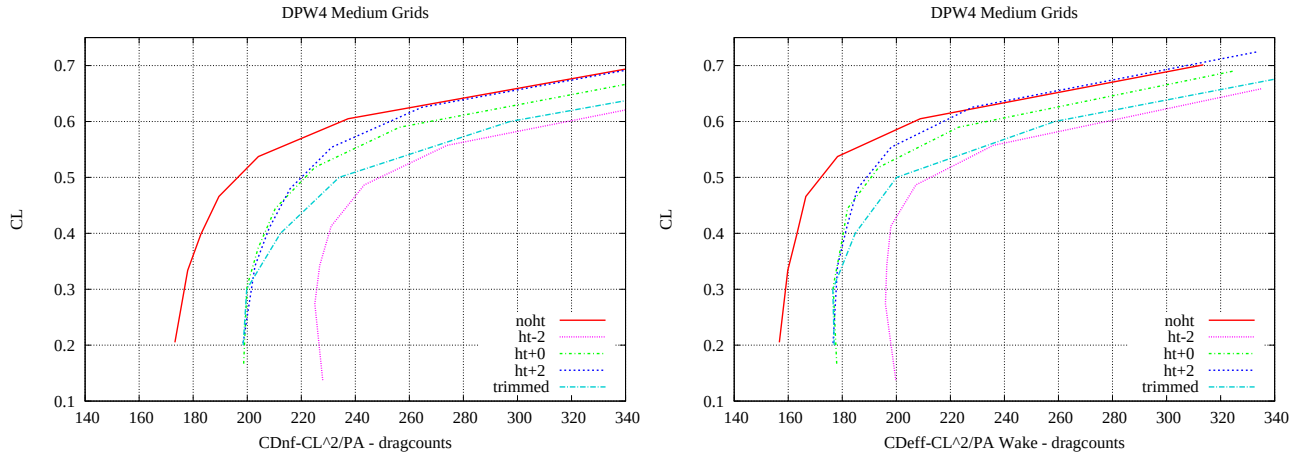

(a) Near Field Drag (b) Effective Drag

Figure 4. Idealized Drag Polars Down Wash Study.

in the CGNS standard. A patch grid block boundary condition was employed downstream of the wing. No grid clustering of the grid at the trailing edges of the wing and horizontal tail was employed. The grid was provided in metric units, and was translated in X-direction compared to the geometry file. Inspection of the aircraft and far-field boundary surfaces showed that these were not entirely closed in X- and Z-direction. This may influence the results of the drag extraction tool. The Ansys grid was obtained in ICEMCFD format, and was the easiest to import. The Boeing grid was provided together with a small code to read the grid and a description of the boundary conditions. Since there were only 4 blocks the boundary conditions were generated by hand. To permit parallel computations the Boeing grid was later split into 30 blocks using an in-house tool. The Boeing grid had small blocks downstream of the trailing edges of wing and horizontal tail with collapsed surfaces on the sides. As with the Airbus grid no grid clustering was used on the trailing edges of wing and horizontal tail. The Boeing grid was rotated 90^o around the X-axis. This was corrected after the calculations to permit the use of the drag extraction tool which assumes an aerodynamic coordinate system. The Boeing grid was not entirely aligned with the symmetry plane, and the aircraft and far field surfaces were not closed in X- and Z-directions. Finally the far field boundaries were very close to the body (3 fuselage lengths upstream of the body, 4 fuselage lengths downstream of the body and 1 span from the symmetry plane). The theory behind the drag extraction tool assumes that far field boundaries are located far from the body in order that perturbations are small. This assumption is not valid for the Boeing grid. Combined with the misalignment of the grid in the symmetry plane and the not closed aircraft and far field integration surfaces it is necessary to express doubts on the results of the drag extraction tool obtained for this grid. The Jaxa grid was obtained in plot3d format and additional files were provided for the boundary conditions. A program was written to convert the boundary condition file to the format used by NSMB. The Zeus grids was received in CGNS format, and could be relatively easy converted to the format used by NSMB. The Zeus grid had some problems with block interfaces which were not exactly matching.

All calculations were made in the metric coordinate system using SI units. The calculation strategy and calculation set-up were the same for all calculations except for the calculations on the cfse-ra grid for which 2 levels of grid sequencing was used. On this grid only 3500 time steps were made on the finest grid level, while 6000 time steps were made on all other grids.

From Table 4 it can be seen that the ZEUS grid was the finest and had the largest number of cells on the surface. The Jaxa grid was the coarsest, but still had more cells on the surface than the Ansys, Boeing and cfse-ra grids. Figure 5 shows comparisons of the different grids on the wing. The Airbus, Boeing and Jaxa grid employed grid clustering near the leading and trailing edges of the wing. The Zeus grid has a fine mesh in this region, but specific grid clustering was not employed. The cfse-ra grid was slightly more refined than the Ansys grid in these regions. The cfse-ra grid was very fine on the fuselage, more than the other grids.

Similar observations can be made for the horizontal tail, where the Airbus and Boeing grid had grid points clustered near the leading and trailing edges. The Jaxa grid was rather coarse here, with little grid point

Participant	Mcells	surface cells	blocks	type
Airbus	12.6	126'000	167	H-grid
Ansys	10.8	73'000	241	O-grid
Boeing	11.0	64'000	4	H-grid
cfse-ra	11.3	80'000	327	H-grid
Jaxa	9.0	100'000	283	C-grid
Zeus	15.4	185'000	326	H-grid

Table 4. Characteristics different multi block structured grids used in the DPW4 workshop.

clustering. The Zeus grid was uniformly refined, without specific clustering. Figure 6 shows figures of the different grids in this region. In Fig. 6(a) the patch grid block interface can be seen on the fuselage for the Airbus grid.

FIGURE 7 shows the idealized drag polar calculated using the near field and effective drag on the different grids. The following observations can be made:

- the computed lift on Zeus grid is lower compared to results on the other grids;
- for low values of the C_L, the spread in computed idealized drag based on the near field drag is about 20 drag counts, while it is reduced to about 6 drag counts using the effective drag;
- except for the results on the Zeus grid, it can be observed that computed C_L values are close for all grids;
- the computed idealized drag on the Boeing grid is higher compared to the results on the other grids (except for the Zeus grid). This can probably be attributed to the grid which is not suitable for use with the drag extraction tool.

FIGURE 8 shows the computed viscous, wave and spurious drag polars for the different grids. For low values of the C_L the viscous drag should vary little, and this is observed on all grids except the Boeing grid. The computed wave drag is small, and comparable on all grids except the Zeus grid. Spurious drag levels are the highest on the cfse-ra grid, and the lowest on the Boeing grid although this latter result needs to be interpreted with care for reasons discussed before.

THE drag extraction tool includes 2 methods to compute the induced drag. The first method which is theoretically exact uses the balance between near field drag on one hand, and the sum of viscous, wave, spurious and induced drag on the other hand, see Eq. 33. The viscous, wave and spurious drag components are calculated by integration of Eq. 27 over respectively the viscous, wave and spurious regions. The near field drag is computed from the integration of the pressure and shear stress forces over the aircraft surface, and the unknown induced drag follows from the difference between near field drag and the sum of viscous, wave and spurious drag. The result is shown in Fig.9(a). An alternative method is to compute the induced drag from Eq. 25 with the velocity difference computed from Eq. 35 and the result is shown in Fig. 9(b). Several observations can be made

- for the alternative method the computed induced drag is almost independent of the grid used;
- the induced drag computed using the standard method shows a small spread in results for different grids;
- induced drag levels computed with the standard method are slightly higher compared to the alternative method. Differences are in the order of 5 to 10 drag counts.

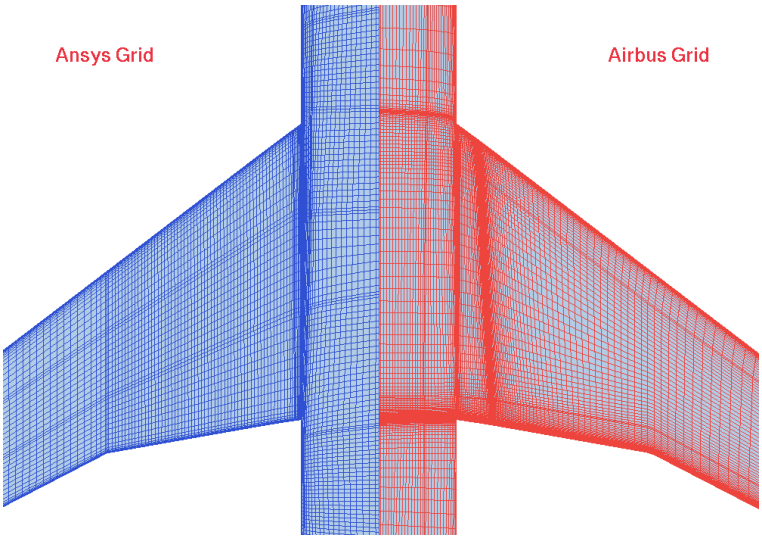

(a) Comparison Airbus and Ansys Grid

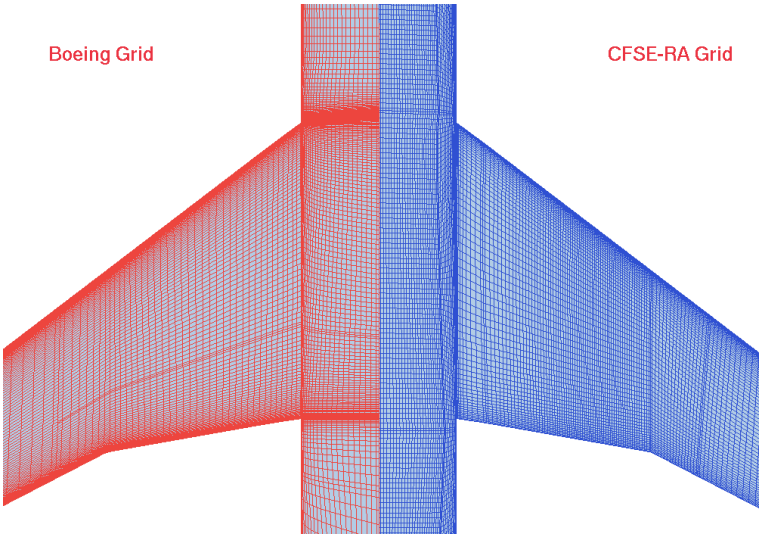

(b) Comparison Boeing and cfse-ra Grid

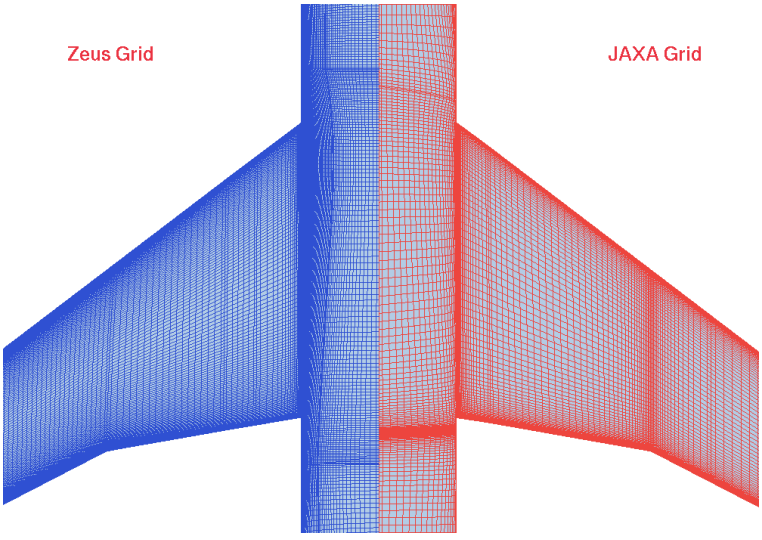

(c) Comparison Jaxa and Zeus Grid

Figure 5. Comparison different grids near the wing.

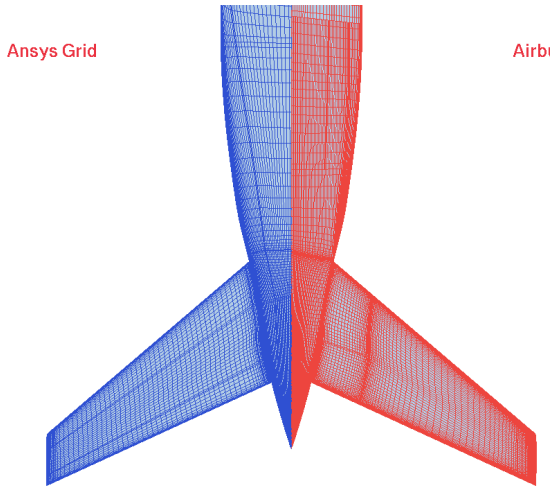

(a) Comparison Airbus and Ansys Grid

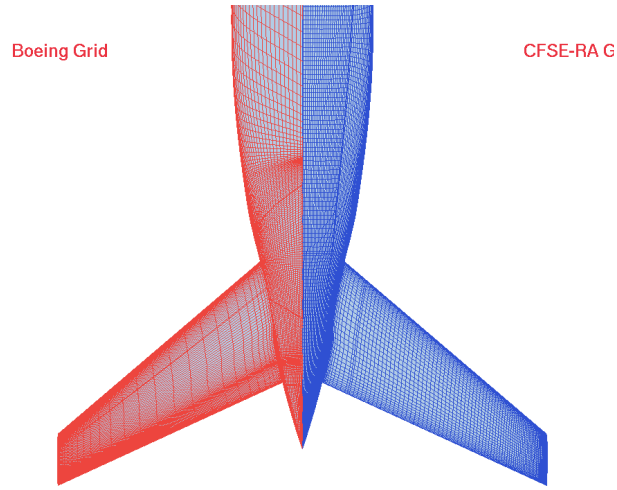

(b) Comparison Boeing and cfse-ra Grid

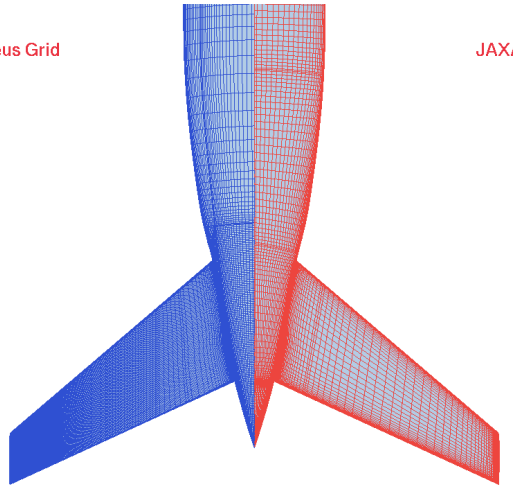

(c) Comparison Jaxa and Zeus Grid

Figure 6. Comparison different grids near the horizontal tail.

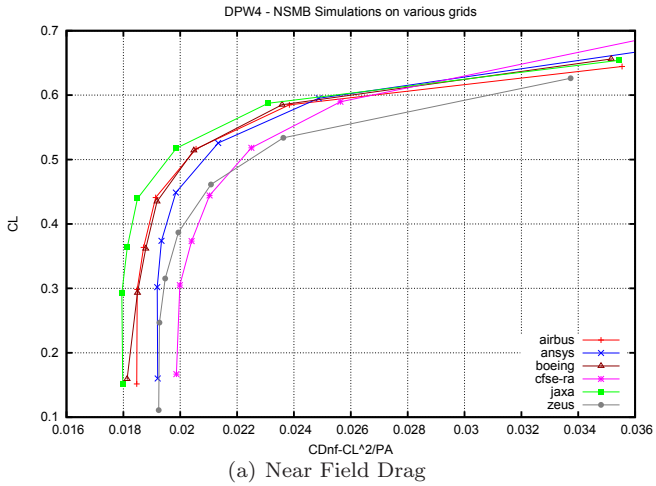

(a) Near Field Drag

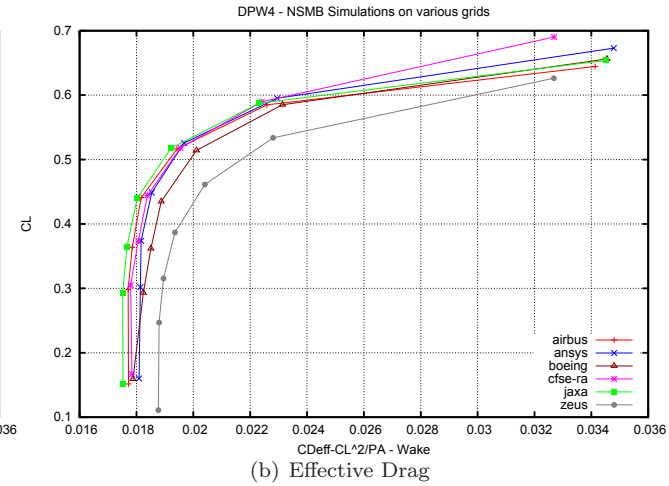

(b) Effective Drag

Figure 7. Idealized Drag Coefficient in Drag counts.

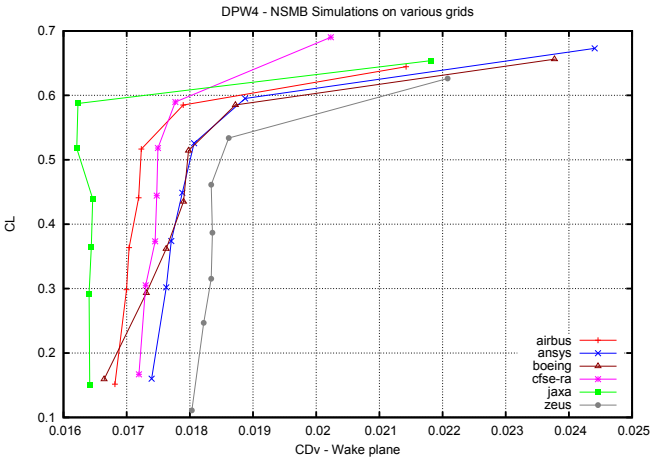

(a) Viscous Drag

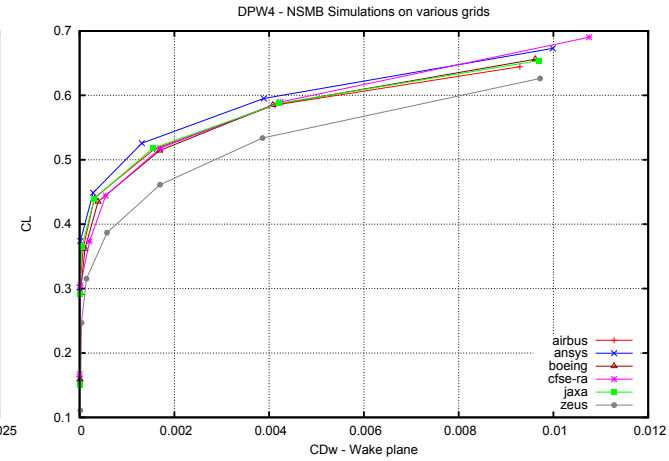

(b) Wave Drag

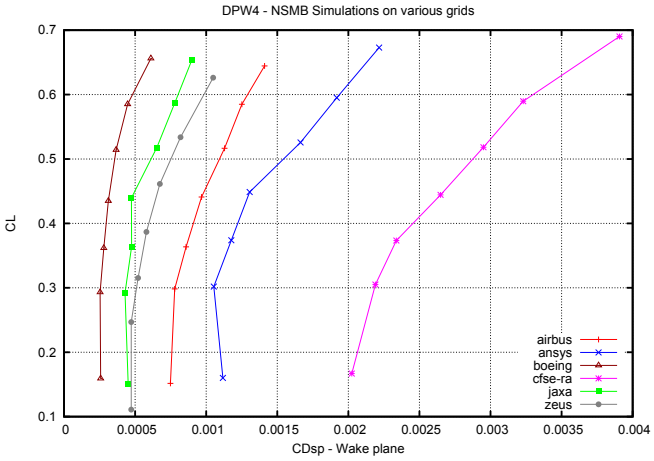

(c) Spurious Drag

Figure 8. Viscous, Wave and Spurious drag polars.

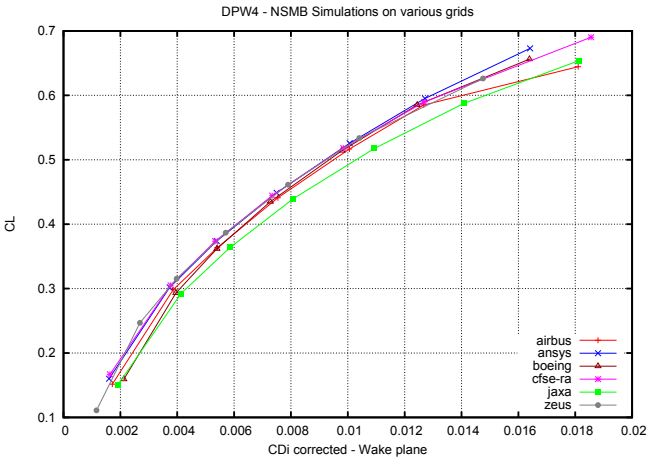

(a) Standard Method

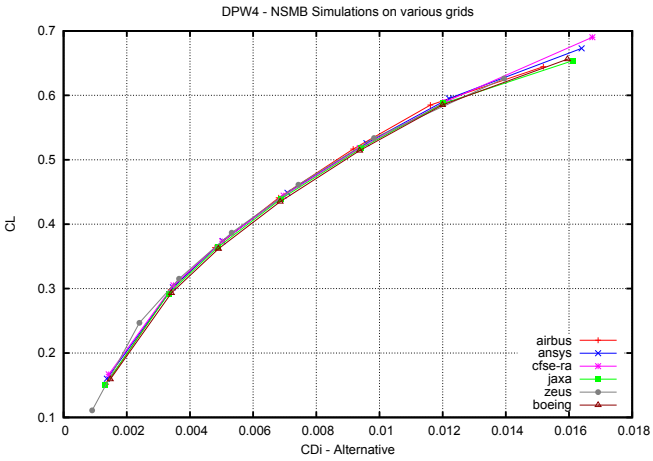

(b) Fom Eq. 25

Figure 9. Induced Drag Polars.

Figure 10 shows a zoom of the idealized drag polars computed using the effective drag coefficient. If it is kept in mind that the results obtained on the Boeing grid needs to be treated carefully, and that the results on the Zeus grid are doubtful, one observes that the results computed on the other 4 grids are close. Differences in idealized drag are in the order of 6 drag counts, despite the large differences in grids used.

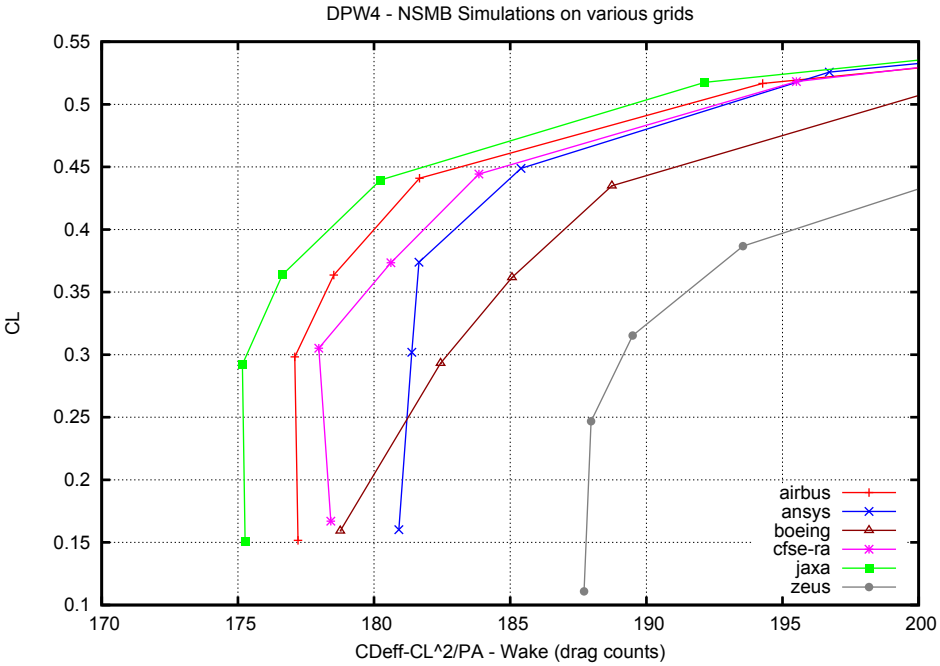

Figure 10. Zoom of computed effective drag polars.

THE computed C_p on 4 wing stations and 1 horizontal tail station using the 6 grids are shown in Fig. 11. The results on the Zeus grid differ from the other results, the shock location is not well captured. There are some small differences in C_p on the cfse-ra and Ansys grid compared to the other grids, in particular near the wing tip (Wing Section 16). The origin of these differences is probably the absence of sufficient grid clustering near the trailing edge of the wing for these grids.

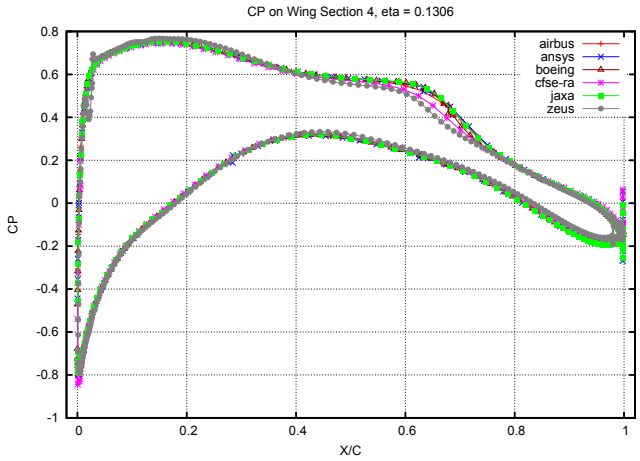

(a) Wing station 4

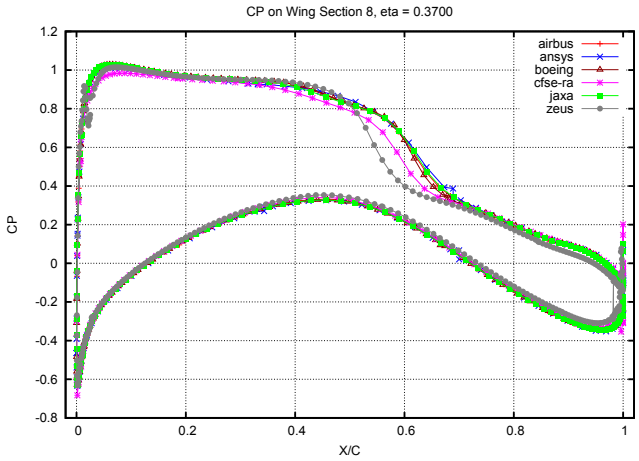

(b) Wing station 8

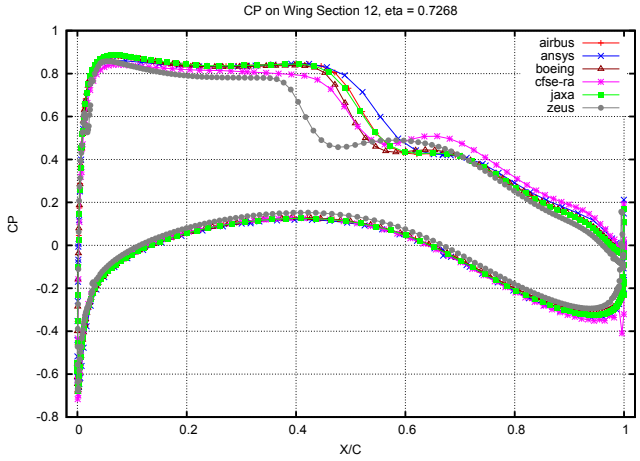

(c) Wing station 12l

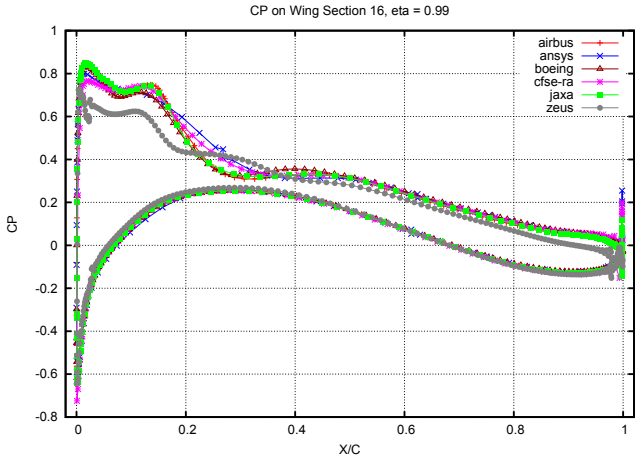

(d) Wing station 16

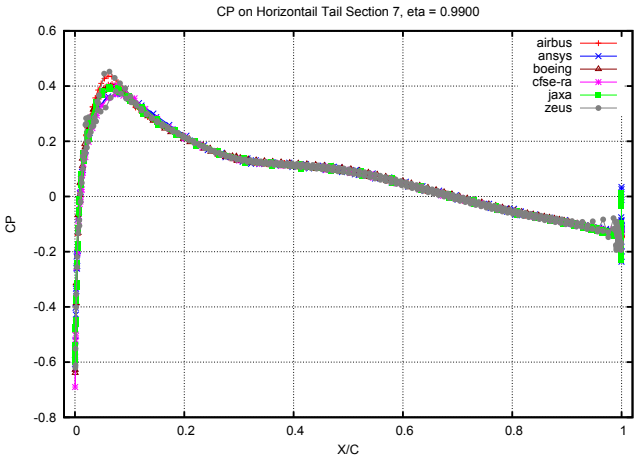

(e) Horizontal tail station 7

Figure 11. C_p **on cuts on the wing and horizontal tail,** $\alpha = 2.5$**.**

Figure 12 shows the pitching moment coefficient. The slope of the different curves are comparable except for the highest value of the C_L. point. This point corresponds to $\alpha = 4.0^o$ and flow separations near the wing trailing edge and on the horizontal tail have become important. Grid resolution is an important parameter which influence the resolution of these flow separations, and one can observe that the results obtained with grids which employ clustering near the trailing edge are close together. The results obtained on the cfse-ra and Zeus grid differ from the other results, likely due to insufficient grid clustering.

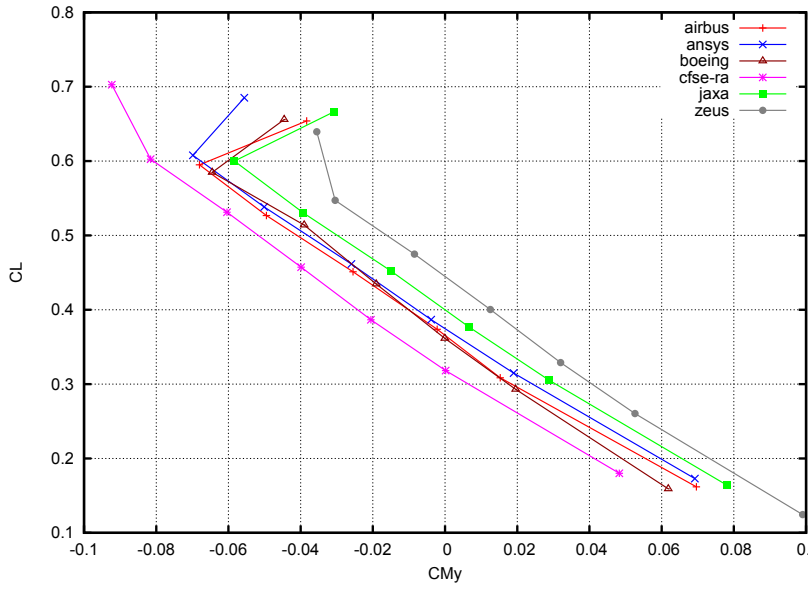

Figure 12. Pitching moment coefficient on different grids.

V. Conclusions

CFD simulations using the NSMB code were made for the DPW4 test case. Drag results were analyzed using the traditional near field drag analysis and using a drag extraction tool based on a far-field analysis. This latter tool permits to remove spurious drag components introduced by the grid and the numerical scheme from the computed drag.

Using the drag extraction tool on the DPW4 results for the grid convergence shows that the effective drag is lower than the near field drag, and that the effective drag converges faster with increasing grid density.

The results for the down wash study showed that the iealized drag computed using the drag extraction tool is about 20 drag counts lower compared to the near field drag.

After the DPW4 workshop computations were made on the different multi block structured grids provided by other participants for the configuration with zero horizontal tail deflection. The results of these computations were analyzed using the drag extraction tool. The results on the Zeus grid were strange, leading to too low values of the lift coefficient C_L probably due to a bad capturing of the shock wave on the wing. The results on the Boeing grid needed to be interpretated with care due to the fact that far field boundaries were extremely close to the aircraft geometry. The results on the other 4 grids showed that the spread in idealized drag coefficient using near field drag was about 20 drag counts, which was reduced to about 6 drag counts when using the effective drag. Deficiencies in the grid, as for example the absent of sufficient clustering at leading and trailing edges of wing and horizontal tail, influenced the near field drag, but had apparently little influence on the effective drag. These results demonstrate the importance of using a drag extraction tool.

References

[1]Levy, D.W. et al., Summary of Data from the First AIAA CFD Drag Prediction Workshop. AIAA Paper 2002-0841, 40th AIAA Aerospace Sciences Meeting 2002.

[2]Redeker, G., DLR-F4 Wing-Body Configuration A selection of Experimental Test Cases for the Validation of CFD Codes, AGARD Report AR-303, 1994.

[3]Brodersen, O. and Sturmer, A., Drag Prediction of Engine-Airframe Interference Effects using Unstructured Navier-Stokes Calculations, AIAA 2001-2414, 19th AIAA Applied Aerodynamics Conference, 2001.

[4]Laflin, K.R. et al., Data Summary from Second AIAA Computational Fluid Dynamics Drag Prediction Workshop, Journal of Aircraft, Vol. 42, No. 5, 2005.

[5]Vassberg J.C. et al., Abridged Summary of the Third AIAA Computational Fluid Dynamics Drag Prediction Workshop, Journal of Aircraft, Vol. 45, No. 3, 2008.

[6]Brodersen , O. et al., DLR Results from the Third AIAA Computational Fluid Dynamics Drag Prediction Workshop, Journal of Aircraft, Vol. 45, No. 3, 2008

[7]Mavriplis, D.J. et al., Grid Quality and Resolution Issues from the Drag Prediction Workshop Series, Journal of Aircraft, Vol. 46, No. 3, 2009.

[8]Laflin, K.R., AIAA CFD Drag Prediction Workshop: An Overview, 25th ICAS Conference, 2006.

[9]Vassberg, J.C. et al., Development of a Common Research Model for Applied CFD Validation Studies, AIAA-2008-6919, 2008.

[10]Destarac D., Far-Field/Near-Field Drag Balance and Applications of Drag Extraction in CFD, VKI Lecture Series CFD-Based Aircraft Drag Prediction and Reduction, VKI LS 2003-02, 2003.

[11]Destarac D. and van der Vooren J., Drag/thrust analysis of jet-propelled transonic transport aircraft: Definition of physical drag components, Aerospace Science and Technology, Vol. 8, 2004, pp. 545-556.

[12]Esquieu, S., Numerical Simulation and Drag Extraction using Patched Grid Calculations. AIAA 2003-1238, 2003.

[13]Vooren J. van der and Slooff, J.W., CFD Based Drag Prediction; State of the Art, Theory, Prospects, NLR TP-90247 U, 1990, AIAA Professional Studies Series, Course on Drag-Prediction and Measurement, 1990.

[14]Tognaccini T., Methods for Drag Decomposition, Thrust-Drag Bookkeeping from CFD Calculations, VKI Lecture Series CFD-Based Aircraft Drag Prediction and Reduction, VKI LS 2003-02, 2003.

[15]Esquieu, S., Evaluation de la Trainee d'un Avion de Transport a partir de Calculs Numeriques de Mecanique des Fluides, Ph.D Thesis (in French), University of Bordeaux, 2003.

[16]Van Dam C.P., Recent experience with different methods of drag prediction, Progress in Aerospace Sciences, Vol. 35, 1999, pp. 751-798.

[17]Yamazaki W., Matsushima K. and Nakahashi K., Aerodynamic Design Optimization using the Drag-Decomposition Method, AIAA Journal, Vol. 46, May 2008, pp. 1096-1106.

[18]Yamazaki W., Matsushima K. and Nakahashi K., Drag prediction, decomposition and visualization in unstructured mesh CFD solver of TAS-Code, Internation Journal for Numerical Methods in Fluids, Vol. 37, 2008, pp. 417-436.

[19]Vos JB, Rizzi AW, Corjon A, Chaput E, Soinne E. Recent Advances in Aerodynamics inside the NSMB (Navier-Stokes Multiblock) Consortium. AIAA paper 98-0225, 1998.

[20]Guillaume M., Gehri A., Stephani P., Vos J., Manadanis G., Fluid Structure Interaction Simulation on the F/A-18 Vertical Tail, AIAA-2010-4613, Chicago, 2010.

[21]Menter, F.R., Zonal Two Equation $k-\omega$ Turbulence Models for Aerodynamic Flows, AIAA paper, vol. 93-2906, 1993